Pergamon

Int. J. Heat Mass Transfer. Vol. 38, No. 18, pp. 3455–3473, 1995

0017–9310/95 $9.50+0.00

0017–9310(95)00054–2

A numerical study of the combined effects of microsegregation, mushy zone permeability and flow, caused by volume contraction and thermosolutal convection, on macrosegregation and eutectic formation in binary alloy solidification

M. C. SCHNEIDER and C. BECKERMANN†

Department of Mechanical Engineering, The University of Iowa, Iowa City, IA 52242, U.S.A.

(*Received* 17 *February* 1994 *and in final form* 19 *January* 1995)

Abstract—Numerical simulations of the columnar dendritic solidification of a Pb–20 wt% Sn alloy in a square cavity cooled from one side and fed by a rectangular riser are reported. Overall macrosegregation patterns predicted using Scheil and lever-rule type microsegregation models are found to be similar, although the predicted eutectic fraction is significantly higher with the Scheil-type model. The choice of mushy zone permeability function significantly affects the predicted number, length and orientation of segregated channels. The inclusion of shrinkage-driven flow leads to the prediction of the well-known inverse macrosegregation pattern. However, macrosegregation caused by thermosolutal convection readily masks the inverse segregation. The microsegregation models predict different solid concentrations and eutectic fractions, leading to different solid density distributions which, in turn, cause differences in the extent of contraction-driven flow.

1. INTRODUCTION

In recent years, much time and effort has been expended trying to develop accurate models, as well as efficient numerical algorithms to solve the model equations, for studying the transport phenomena that occur during alloy solidification. The aim of these studies is to develop predictive capabilities that allow for the design of defect-free castings. Numerical solution of the conservation equations in macroscopic alloy solidification models has shown the capability of such models to predict the development of an irregular liquidus front, local remelting of solid, channels in the mushy zone and complicated macrosegregation patterns, for the solidification of salt-water solutions [1–3] as well as metal alloys [5–7].

In applying alloy solidification models, several assumptions are typically introduced to simplify the solution of the conservation equations. They include: thermal equilibrium, a well-mixed liquid, and complete (i.e. infinitely fast) species diffusion in the solid within a small volume element; an isotropic permeability in the mushy zone; and constant and equal phase densities (i.e. neglecting contraction-driven flow) with the Boussinesq approximation used to model buoyancy-driven flow. In order better to evaluate and understand macroscopic solidification models, the effects of these assumptions on the resulting model predictions need to be investigated. Towards that goal, the objective of this study is threefold. First, a comparison is made between macrosegregation and eutectic volume fraction patterns predicted when there is assumed to be either complete or no solute diffusion microscopically in the solid. A comparison is also made between predictions obtained when using different mushy zone permeability relations, with the focus on the necessity of considering the anisotropy of the permeability and of accurately specifying the permeability at high liquid fractions. Finally, the combined effects of flow due to buoyancy and volume contraction (caused by solid/liquid density differences as well as density variations with temperature and concentration) are investigated. The model predictions used in all of the comparisons are for the columnar dendritic solidification of a Pb–20 wt% Sn alloy in a square cavity cooled from one side and fed by a rectangular riser.

The assumption of infinitely fast solute diffusion in the solid on a microscopic scale (i.e. a lever-rule type model) can be considered as one limiting case describing solid microsegregation. Then, a second limiting case is described by assuming no microscopic solute diffusion in the solid (i.e. a Scheil-type model). Several studies have employed a Scheil-type model in calculating macrosegregation during alloy solidification [3, 5, 8, 9]. In the only study that directly compared

† Author to whom correspondence should be addressed.

NOMENCLATURE

a	lattice parameter [m]
C	concentration [wt% Sn]
d	dendrite arm spacing [m]
D	mass diffusivity [$m^2 s^{-1}$]
g	liquidus curve equation
$\mathbf{g}$	acceleration of gravity [$m s^{-2}$]
h	enthalpy [$J kg^{-1}$]
k	thermal conductivity [$W m^{-1} K^{-1}$]
$\mathbf{K}^{(2)}$	second-order permeability tensor [m^2]
K	permeability [m^2]
l	length scale [m]
m_l	liquidus curve slope [K wt% Sn)
p	pressure [$N m^{-2}$]
S	interfacial area concentration [m^{-1}]
t	time [s]
t_f	local solidification time [s]
T	temperature [K]
U	heat transfer coefficient [$W m^{-2} K^{-1}$]
$\mathbf{v}$	velocity vector [$m s^{-1}$]
x	x direction [m]
y	y direction [m].

Greek symbols

Γ	Gibbs–Thomson coefficient [mK]
ε	volume fraction
κ	segregation coefficient [wt%/wt%]
μ	kinematic viscosity [$kg m^{-1} s^{-1}$]
ρ	density [$kg m^{-3}$]
Ψ	a quantity of a phase
$\langle\Psi_k\rangle^k$	volume average of Ψ in phase k.

Subscripts

e	eutectic
i	interfacial
j	species transfer
k	phase k
l	liquid
mix	mixture
o	initial, constant
s	solid
α	alpha phase
γ	gamma phase
η	normal to dendrite
ξ	perpendicular to dendrite
1	primary dendrite arm
2	secondary dendrite arm.

Superscripts

Pb	pure lead
Sn	pure tin
t	transpose of a tensor
$\bar{}$	interfacial average.

macrosegregation patterns [3], it was determined that the general behavior for the two limiting cases was qualitatively similar, with the predicted macrosegregation for the case of no solute diffusion slightly worse than that for complete solute diffusion. For diffusion-dominated solidification, the movement of the liquidus isotherm was shown to differ only slightly [10, 11], while the final volume fraction of eutectic was quite different for the two cases [11]. In the model used here, the conservation equations are written in a general form that easily accommodates both the assumptions of infinitely fast and no solute diffusion in the solid microscopically. In addition, the eutectic reaction is considered in detail, which is important since in Pb–Sn alloys the primary and eutectic solid specific heats differ by 27% and their densities differ by 17% [12, 13]. Very recently, Sundarraj and Voller [14] coupled the numerical solution of mass diffusion equations for the solid and liquid phases on a microscopic scale (including finite rate diffusion in the solid and dendrite arm coarsening) with one-dimensional calculations of the macrosegregation which results from contraction-driven flow. The predictions of this sophisticated model showed that the eutectic fraction decreased with increasing back diffusion in the solid, and that this influenced the predicted macrosegregation profile.

Since the permeability of the mushy zone has a significant effect on interdendritic fluid flow, and therefore on the transport of heat and mass on the macroscopic level, it must be accurately described in a solidification simulation. However, the uncertainty in experimentally measured permeabilities is large, and such measurements are practical only for a limited range of liquid fractions (between 0.15 and 0.65) [15]. Nevertheless, it has been shown that the directional nature of the columnar dendrites in the mushy zone causes the permeability to be anisotropic [15], and neglecting the anisotropy in solidification simulations can have an effect on the convective flow during solidification [16, 17] which leads to significant differences in the prediction of the growth of double diffusive layers, remelting of solid and macrosegregation [17]. In this study a comparison is made of the flow and macrosegregation patterns that are predicted when using two permeability expressions that are available in the literature.

Including contraction-driven flow, in addition to buoyancy driven flow, in solidification simulations has also received attention recently. Chiang and Tsai [18] investigated the interaction of buoyancy and shrinkage driven flow during the solidification of a 1% Cr-steel, but did not consider species transport. Tsai and co-workers [19–21] obtained good agreement between predicted and measured inverse segregation profiles for unidirectional solidification of an Al–Cu alloy, where flow was due to contraction only. Sundarraj and Voller [14] showed that such comparisons can be

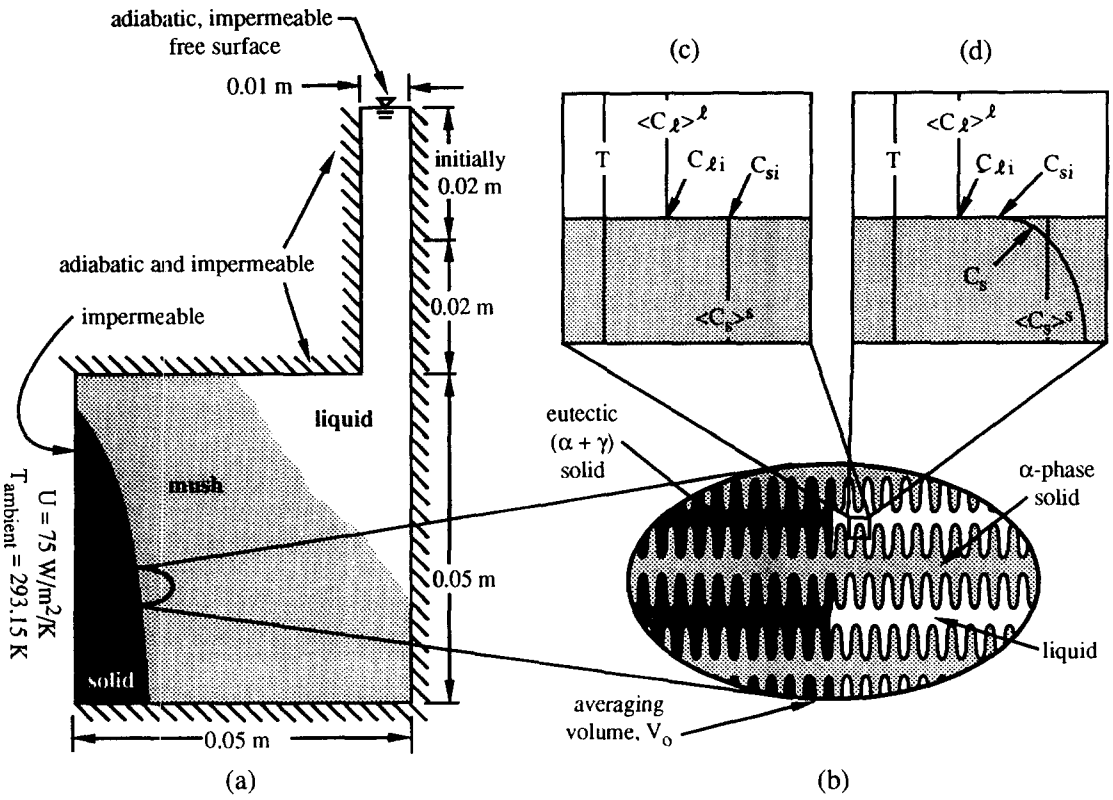

Fig. 1. Schematic illustrations of: (a) the domain and boundary conditions used in the solidification simulations, (b) a typical averaging volume, and the microscopic temperature and concentration profiles for (c) infinitely fast microscopic solid solute diffusion and (d) no microscopic solid solute diffusion.

ambiguous if microsegregation, coarsening and eutectic formation are not rigorously accounted for. Xu and co-workers [8, 22, 23] solved the complete set of conservation equations with both buoyancy- and contraction-driven flow for the solidification of an Al–Cu alloy. Although the computational grid used in the simulations was too coarse to capture double-diffusive layering and local remelting of solid, reasonable agreement with experimental results was obtained. Krane and Incropera [24] examined the combined effects of shrinkage- and buoyancy-driven flow on macrosegregation formation during the solidification of a Pb–19.2 wt% Sn alloy, and determined that shrinkage effects become increasingly important with increasing cooling rates. However, because a lever-rule type microsegregation model was used, little or no eutectic solid was predicted to form. The results presented in this study include the effects of flow due to both buoyancy and solidification shrinkage, coupled with two limiting microsegregation cases that predict different eutectic fractions.

2. MODEL DESCRIPTION

As illustrated in Fig. 1, the physical situation under consideration is the solidification of a Pb–Sn alloy in a two-dimensional 5 cm by 5 cm cavity with an attached 1 cm wide by 4 cm high riser. All the walls of the cavity, as well as the free surface at the top of the riser, are impermeable. The cavity is convectively cooled at the left wall with an overall heat transfer coefficient of 75 W m^{-2} K^{-1} and an ambient temperature of 293 K, while the remaining walls and the free surface are adiabatic. Surface tension effects at the free surface in the riser are neglected, and a no-slip boundary condition is applied at all of the walls. The alloy is initially quiescent with a uniform composition of Pb–20 wt% Sn and a uniform temperature of 576 K (25 K of superheat). Thermophysical properties for the Pb–Sn system are summarized in Table 1.

The model described here is, in essence, a generalization of the model used by Beckermann and Viskanta [2], and can be directly obtained from the volume-averaged two-phase model of alloy solidification presented by Ni and Beckermann [25]. A detailed description of the derivation of the model equations is available elsewhere [26–28] so that only a brief discussion is included here. There are assumed to be at most three phases present: liquid (denoted by a subscript l), alpha-solid (subscript α) and gamma-solid (subscript γ). Alternatively, one could consider liquid, primary (α- or γ-) solid and eutectic solid. The primary solids are considered separately here because the eutectic solid is, in reality, made up of α- and γ-solid, and because this approach is more general than calculating a single eutectic solid fraction. In all the

Table 1. Phase diagram relations, thermophysical properties, mushy zone permeabilities and dendrite arm spacing relations for the Pb–Sn system

Liquidus curve (K) [13]

$$T = \begin{cases} 600.8 - 2.8290C_l + 2.5088\times10^{-2}C_l^2 - 2.7597\times10^{-4}C_l^3 & \text{for } C_l \leqslant 61.9 \\ 229.4 + 7.7091C_l - 0.091235C_l^2 + 4.1752\times10^{-4}C_l^3 & \text{for } C_l > 61.9 \end{cases}$$

Segregation coefficients (wt% Sn/wt% Sn) [13]

$$\kappa_\alpha = 0.8273 - 4.2208\times10^{-2}C_l + 1.9680\times10^{-3}C_l^2 - 5.1866\times10^{-5}C_l^3 + 6.8075\times10^{-7}C_l^4 + 3.4568\times10^{-9}C_l^5;$$

$$\kappa_\gamma = 85.83/C_l + 0.33878 - 4.4858\times10^{-3}C_l + 2.0146\times10^{-5}C_l^2$$

Phase enthalpies (J/kg) [12]

$$h_l = [0.079393C_l + 156.81]T - 7.452\times10^{-5}(100-C_l)T^2 - 25490C_lT^{-1} + 228.122C_l + 53769C_l(100-C_l)/(11869+88.51C_l) - 978.2C_l(100-C_l)(325.89C_l - 11869)/(11869+88.51C_l)^2 - 27747.9;$$

$$h_\alpha = [113.678 + 0.682376C_\alpha]T + [2.3507\times10^{-2} + 5.2996\times10^{-5}C_\alpha]T^2 + 214.25C_\alpha + 47590C_\alpha(100-C_\alpha)/(11869+88.51C_\alpha) - 22930C_\alpha(100-C_\alpha)(325.89C_\alpha - 11869)/(11869+88.51C_\alpha)^2 - 36028;$$

$$h_\gamma = [113.678 + 0.682376C_\alpha]T + [2.3507\times10^{-2} + 5.2996\times10^{-5}C_\alpha]T^2 - 273.6C_\gamma + 196930C_\gamma(100-C_\gamma)/(11869+88.51C_\gamma) - 33670$$

Phase densities (kg m^{-3}) [13]

$$\rho_l = \{(1.9095\times10^{16} + 3.3211\times10^{14}C_l + 9.014\times10^{11}C_l^2 + 4.0665\times10^9C_l^3) - (2.1363\times10^{12} + 3.9986\times10^{10}C_l - 1.6899\times10^8C_l^2 + 1.8477\times10^6C_l^3)T\}/(88.51C_l + 11869)^3;$$

$$\rho_\alpha = 1.6334\times10^{-20}/(88.51C_\alpha + 11869)a_\alpha^{-3} \quad \text{where} \quad a_\alpha = 4.8910\times10^{-10} + 1.9625\times10^{-14}T - \frac{2.9328\times10^{-9}C_\alpha}{88.51C_\alpha + 11869};$$

$$\rho_\gamma = 2.9940\times10^{-20}/(88.51C_\gamma + 11869)a_\gamma^{-3} \quad \text{where} \quad a_\gamma = \frac{1.1305\times10^{-8}}{(6.724\times10^{-5}T^2 + 0.1270T + 7262)^{1/3}} - \frac{1.6795\times10^{-8}(100-C_\gamma)}{88.51C_\gamma + 11869}$$

Phase thermal conductivities (W m^{-1} K^{-1}) [5, 38]

$$\ln(k_l) = \frac{C_l}{100}\ln(k_l^{Sn}) + \frac{100-C_l}{100}\ln(k_l^{Pb}) \quad \text{where} \quad \ln(k_l^{Sn}) = 0.85337 + 0.4109\ln(T)$$

and $\ln(k_l^{Pb}) = -2.0725 + 0.7521\ln(T)$;

$$\ln(k_s) = \frac{C_s}{100}\ln(k_s^{Sn}) + \frac{100-C_s}{100}\ln(k_s^{Pb}) \quad \text{where} \quad \ln(k_s^{Sn}) = 4.5422 - 0.1708\ln(T)$$

and $\ln(k_s^{Pb}) = 3.7507 - 0.1708\ln(T)$

and $C_s = (\varepsilon_\alpha\rho_\alpha C_\alpha + \varepsilon_\gamma\rho_\gamma C_\gamma)/(\varepsilon_\alpha\rho_\alpha + \varepsilon_\gamma\rho_\gamma)$

Viscosity (kg m^{-1} s^{-1}) [39]

$$\mu_l = (118.69C_l\mu_l^{Sn} + 207.2C_l\mu_l^{Pb})/(88.51C_l + 11869)$$

where $\mu_l^{Sn} = 2.75\times10^{-5}(\rho_l^{Sn})^{1/3}\exp\{0.0885\rho_l^{Sn}/T\}$

and $\mu_l^{Pb} = 2.54\times10^{-5}(\rho_l^{Pb})^{1/3}\exp\{0.0863\rho_l^{Pb}/T\}$

Liquid mass diffusivity (m^2 s^{-1}) [40]

$$D_l = 3.0\times10^{-9}$$

Permeability parallel to primary dendrite arms (m^2) [5, 15, 32]

$$K_{\xi\xi} = \begin{cases} [4.53\times10^{-4} + 4.02\times10^{-6}(\varepsilon_l + 0.1)^{-5}]\dfrac{d_1^2\varepsilon_l^3}{(1-\varepsilon_l)} & \text{for } \varepsilon_l < 0.7 \\ 0.07425d_1^2[-\ln(1-\varepsilon_l) - 1.487 + 2(1-\varepsilon_l) - 0.5(1-\varepsilon_l)^2] & \text{for } \varepsilon_l \geqslant 0.7 \end{cases}$$

Permeability perpendicular to primary dendrite arms (m^2) [5, 15, 33]

$$K_{\eta\eta} = \begin{cases} \left[1.73\times10^{-3}\left(\dfrac{d_1}{d_2}\right)^{1.09}\right]\dfrac{d_2^2\varepsilon_l^3}{(1-\varepsilon_l)^{0.749}} & \text{for } \varepsilon_l < 0.7 \\ 0.03979d_1^2[-\ln(1-\varepsilon_l) - 1.476 + 2(1-\varepsilon_l) - 1.774(1-\varepsilon_l)^2 + 4.076(1-\varepsilon_l)^3] & \text{for } \varepsilon_l \geqslant 0.7 \end{cases}$$

Isotropic permeability (m^2) [6]

$$K_{isotropic} = K_{\xi\xi} = K_{\eta\eta} = K_0\frac{\varepsilon_l^3}{(1-\varepsilon_l)^2} \quad \text{where} \quad K_0 = 2.8\times10^{-11}\,\text{m}^2$$

Primary dendrite arm spacings (m) [41, 42]

$$d_1 = 325.1\times10^{-6}C_0^{0.25}\left[\left(\frac{\partial T}{\partial x}\right)^2 + \left(\frac{\partial T}{\partial y}\right)^2\right]^{-0.25}\left(\frac{\partial T}{\partial t}\right)^{-0.25}$$

Secondary dendrite arm spacings (m) [43]

$$d_2(t_f) = \left(d_2(0)^3 + \int_0^{t_f}\frac{\Gamma D_l}{m_l(\kappa_\alpha - 1)C_l}\,dt\right)^{1/3}$$

where m_l = slope of the liquidus curve

and $\Gamma = 1.0\times10^{-7}\,\text{J m}^{-2}$

model equations. $\langle \Psi_k \rangle^k$ indicates the intrinsic volume average of a quantity Ψ of phase k, and $\bar{\Psi}_{ki}$ indicates an average of a quantity Ψ of phase k over the interfacial area of phase k in the averaging volume.

A number of assumptions are made to simplify the governing equations, including: (i) the solid phases are stationary and rigid so that $\langle \mathbf{v}_\alpha \rangle^\alpha = \langle \mathbf{v}_\gamma \rangle^\gamma = 0$; (ii) all of the phases within an averaging volume are in thermal equilibrium, i.e. $\langle T_\alpha \rangle^\alpha = \langle T_\gamma \rangle^\gamma = \langle T_l \rangle^l = T$; (iii) the liquid within an averaging volume is well mixed so that the interfacial average and volume average concentrations are equal, i.e. $\langle C_l \rangle^l = \bar{C}_{li}$; (iv) microscopic species diffusion in the solid phases is described by one of two limiting cases: (a) complete diffusion, where the interfacial average and volume average concentrations are equal, i.e. $\bar{C}_{si} = \langle C_s \rangle^s$ (where s = α or γ) or (b) no diffusion, where there is a microscopic solute profile in the solid, i.e. $\bar{C}_{si} \neq \langle C_s \rangle^s$ (where s = α or γ); (v) finite-rate macroscopic liquid species diffusion is included, while all macroscopic solid species fluxes are negligible, and all macroscopic species gradients appearing in the mixture energy equation are neglected; (vi) thermodynamic equilibrium exists at the solid–liquid interfaces so that the interfacial temperature and concentrations can be related through the phase diagram, i.e. $T = g(\langle C_l \rangle^l)$ and $\bar{C}_{si}/\langle C_l \rangle^l = \kappa_s(\langle C_l \rangle^l)$ where g is an equation describing the liquidus curve, and κ_s is the equation for the segregation coefficient of solid phase s (where s = α or γ); (vii) gravity is the only body force present, and the dissipative interfacial stress for flow through the porous matrix of columnar dendrites is modeled using the mushy zone permeability in analogy with Darcy's law. Assumptions (ii) through (iv) are illustrated in Fig. 1, and the macroscopic conservation equations are summarized in Table 2. Note that no assumption has been made about the phase densities being constant and/or equal so that the model is capable of predicting melt flow resulting from the volume contraction, or shrinkage, that accompanies solid/liquid phase change, as well as flow resulting from volume variations because of the dependence of the solid and liquid densities on temperature and concentration. The riser attached to the casting (shown in Fig. 1) is used to feed these volume changes, with the method used to handle the movement of the free surface in the riser in the simulations discussed in Section 3.

2.1. *Microscopic solid species diffusion and remelting*

The solid species conservation equation in Table 2 indicates that the rate of change of the volume average solid concentration is balanced by the interfacial transfer of species at the solid/liquid interface. The interfacial species transfer rate consists of two parts: the first due to solidification (change in solid volume fraction) and the second due to species diffusion in the solid at the interface. The interfacial transfer rate due to diffusion is proportional to its driving force (the difference between the interfacial average and volume average concentrations) as well as the interfacial area concentration (S_s), and inversely proportional to a solute diffusion length (l_s^j) which characterizes the resistance to diffusion. If t_f denotes the local solidification time, the quantity $S_s(D_s/l_s^j)t_f$ is a dimensionless diffusion time (Fourier number) [29], and two limiting cases of microscopic solid species diffusion can be considered [30]:

$$S_s \frac{D_s}{l_s^j} t_f \gg 1 \quad s = \alpha, \gamma \tag{1}$$

or

$$S_s \frac{D_s}{l_s^j} t_f \ll 1 \quad s = \alpha, \gamma. \tag{2}$$

Equation (1) implies that the time required for species diffusion in the solid on a microscopic scale is short in comparison with the local solidification time. Then, an order of magnitude analysis of the solid species conservation equation in Table 2 reveals that the volume average solid concentration will be equal to the average interfacial solid concentration, i.e. the solid phases will be solutally well mixed and assumption (iv)(a) will be satisfied. In the absence of macroscopic advection or diffusion of solute, this case reduces to the lever rule, and can be referred to as a lever-rule type model. Conversely, equation (2) means that the time required for microscopic species diffusion in the solid is much longer than the local solidification time. This results in the presence of a microscopic concentration profile within the solid in an averaging volume as noted by assumption (iv)(b), and corresponds to a Scheil-type model. In solving the model equations it is easy to switch between these limiting microsegregation cases simply by setting $S_s\rho_s D_s/l_s^j$ to a suitably large number or to zero, and one objective of the present work is to investigate further the differences in macroscopic model predictions using these two limiting cases to describe solid microsegregation.

During the solidification process, there is the possibility of local remelting of some of the solid that has formed. Since the solid is assumed to be solutally well mixed on a microscopic scale when using equation (1), this presents no difficulty. When using equation (2), however, the presence of a microscopic concentration profile in the solid creates problems during remelting [5, 31]. Since thermodynamic equilibrium exists at the solid/liquid interface during remelting, the interfacial solid concentration will have the composition $\kappa_s\langle C_l \rangle^l$ (where s = α or γ). After remelting, this interfacial solid concentration may not be equal to the composition of the solid near the interface because of the presence of the previously established concentration profile in the solid. The result is a discontinuity in the solid concentration near the interface [31]. In reality there will be some finite rate diffusion in the solid which would smooth out this discontinuity, but a Scheil-type microsegregation model cannot account for solute diffusion. In order to avoid

Table 2. Summary of the macroscopic conservation equations

Mixture mass conservation

$$\frac{\partial}{\partial t}(\varepsilon_l\rho_l)+\nabla\cdot(\varepsilon_l\rho_l\langle\mathbf{v}_l\rangle^l) = -\frac{\partial}{\partial t}(\varepsilon_\alpha\rho_\alpha)-\frac{\partial}{\partial t}(\varepsilon_\gamma\rho_\gamma)$$

Liquid species conservation

$$\varepsilon_l\rho_l\frac{\partial\langle C_l\rangle^l}{\partial t}+\varepsilon_l\rho_l\langle\mathbf{v}_l\rangle^l\cdot\nabla\langle C_l\rangle^l = \nabla\cdot(\varepsilon_l\rho_l D_l\nabla\langle C_l\rangle^l-\varepsilon_\alpha\rho_\alpha\frac{\partial\langle C_\alpha\rangle^\alpha}{\partial t}-\varepsilon_\gamma\rho_\gamma\frac{\partial\langle C_\gamma\rangle^\gamma}{\partial t}$$
$$+[\langle C_l\rangle^l-\langle C_\alpha\rangle^\alpha]\frac{\partial}{\partial t}(\varepsilon_\alpha\rho_\alpha)+[\langle C_l\rangle^l-\langle C_\gamma\rangle^\gamma]\frac{\partial}{\partial t}(\varepsilon_\gamma\rho_\gamma)$$

Solid species conservation ($s = \alpha, \gamma$)

$$\varepsilon_s\rho_s\frac{\partial}{\partial t}(\langle C_s\rangle^s) = [\bar{C}_{si}-\langle C_s\rangle^s]\left\{\frac{\partial}{\partial t}(\varepsilon_s\rho_s)+S_s\frac{\rho_s D_s}{l_s^1}\right\}$$

Mixture energy conservation

$$\varepsilon_l\rho_l\frac{\partial\langle h_l\rangle^l}{\partial T}\bigg|_{\langle C_l\rangle^l}\frac{\partial T}{\partial t}+\varepsilon_l\rho_l\frac{\partial\langle h_l\rangle^l}{\partial T}\bigg|_{\langle C_l\rangle^l}\langle\mathbf{v}_l\rangle^l\cdot\nabla T = \nabla\cdot\{(\varepsilon_l k_l+\varepsilon_s k_s)\nabla T\}-\left(\varepsilon_\alpha\rho_\alpha\frac{\partial\langle h_\alpha\rangle^\alpha}{\partial T}\bigg|_{\langle C_\alpha\rangle^\alpha}+\varepsilon_\gamma\rho_\gamma\frac{\partial\langle h_\gamma\rangle^\gamma}{\partial T}\bigg|_{\langle C_\gamma\rangle^\gamma}\right)\frac{\partial T}{\partial t}$$
$$-\varepsilon_l\rho_l\frac{\partial\langle h_l\rangle^l}{\partial\langle C_l\rangle^l}\bigg|_T\frac{\partial\langle C_l\rangle^l}{\partial t}-\varepsilon_\alpha\rho_\alpha\frac{\partial\langle h_\alpha\rangle^\alpha}{\partial\langle C_\alpha\rangle^\alpha}\bigg|_T\frac{\partial\langle C_\alpha\rangle^\alpha}{\partial t}-\varepsilon_\gamma\rho_\gamma\frac{\partial\langle h_\gamma\rangle^\gamma}{\partial\langle C_\gamma\rangle^\gamma}\bigg|_T\frac{\partial\langle C_\gamma\rangle^\gamma}{\partial t}+\frac{\partial\langle h_l\rangle^l}{\partial\langle C_l\rangle^l}\bigg|_T\left(\varepsilon_l\rho_l\frac{\partial\langle C_l\rangle^l}{\partial t}+\varepsilon_\alpha\rho_\alpha\frac{\partial\langle C_\alpha\rangle^\alpha}{\partial t}+\varepsilon_\gamma\rho_\gamma\frac{\partial\langle C_\gamma\rangle^\gamma}{\partial t}\right.$$
$$\left.-[\langle C_l\rangle^l-\langle C_\alpha\rangle^\alpha]\frac{\partial}{\partial t}(\varepsilon_\alpha\rho_\alpha)-[\langle C_l\rangle^l-\langle C_\gamma\rangle^\gamma]\frac{\partial}{\partial t}(\varepsilon_\gamma\rho_\gamma)\right)+[\langle h_l\rangle^l-\langle h_\alpha\rangle^\alpha]\frac{\partial}{\partial t}(\varepsilon_\alpha\rho_\alpha)+[\langle h_l\rangle^l-\langle h_\gamma\rangle^\gamma]\frac{\partial}{\partial t}(\varepsilon_\gamma\rho_\gamma)$$

Liquid momentum conservation

$$\varepsilon_l\rho_l\frac{\partial\langle\mathbf{v}_l\rangle^l}{\partial t}+\varepsilon_l\rho_l\langle\mathbf{v}_l\rangle^l\cdot\nabla\langle\mathbf{v}_l\rangle^l = -\varepsilon_l\nabla\langle p_l\rangle^l+\nabla\cdot(\varepsilon_l\mu_l\nabla\langle\mathbf{v}_l\rangle^l)$$
$$+\nabla\cdot\{\varepsilon_l\mu_l[\nabla\langle\mathbf{v}_l\rangle^l]^t+\mu_l[\langle\mathbf{v}_l\rangle^l\nabla\varepsilon_l+\nabla\varepsilon_l\langle\mathbf{v}_l\rangle^l]\}$$
$$+\langle\mathbf{v}_l\rangle^l\left(\frac{\partial}{\partial t}(\varepsilon_\alpha\rho_\alpha)+\frac{\partial}{\partial t}(\varepsilon_\gamma\rho_\gamma)\right)-\varepsilon_l^2\mu_l\mathbf{K}^{(2)^{-1}}\langle\mathbf{v}_l\rangle^l+\varepsilon_l\rho_l\mathbf{g}$$

these difficulties, a simple model of remelting that conserves solute is adopted where the average solid concentration is assumed to remain constant during remelting, i.e.

$$\langle C_s\rangle^s = \text{constant during remelting} \quad s = \alpha, \gamma. \quad (3)$$

Similar to the lever-rule type microsegregation model, this is analogous to having a microscopically well mixed solid during remelting with the Scheil-type model. Obviously, this approach does not require the recording of the microscopic solid concentration profile at each node point, as would be necessary in more complicated models of remelting [5, 31]. The present method of handling remelting with the Scheil-type microsegregation model cannot be considered to be realistic, and much future work is required to develop a more accurate method. However, its effects on the predictions presented here are believed to be small.

2.2. *Mushy zone permeability*

The permeability along, $K_{\xi\xi}$, and perpendicular to, $K_{\eta\eta}$, the primary arms in the columnar dendritic mush are not equal, and $K_{\xi\xi}$ and $K_{\eta\eta}$ will be functions of the primary and secondary dendrite arm spacings, as well as the liquid volume fraction [15]. The dendrites are assumed to grow opposite the flow of heat so the angle between the primary arms and the coordinate axes can be determined from the temperature gradient. The functions for $K_{\xi\xi}$ and $K_{\eta\eta}$ given in Table 1 are those used by Felicelli *et al.* [5], but include a dependence on the dendrite arm spacings. These permeabilities are based on experimental measurements for low liquid fractions [15] ($\varepsilon_l < 0.7$) and are based on analytical solutions for flow through arrays of cylinders for high liquid fractions [32, 33]. Also listed in Table 1 is an isotropic permeability relation, based on the Blake–Kozeny model, that has been used extensively in solidification simulations, with the constant K_0 representative for the Pb–Sn alloys studied in this paper [6]. It is important to realize that this isotropic permeability is not the geometric mean of the anisotropic permeabilities, as used by Yoo and Viskanta [17], and that variations with the dendrite arm spacings are neglected.

Figure 2 shows the variation of $K_{\xi\xi}$ and $K_{\eta\eta}$, as well as the isotropic permeability, with liquid fraction. The first observation that can be made is that the anisotropic permeabilities jump by nearly a factor of 100 at the transition point ($\varepsilon_l = 0.7$) between the experimental and analytical permeability expressions.

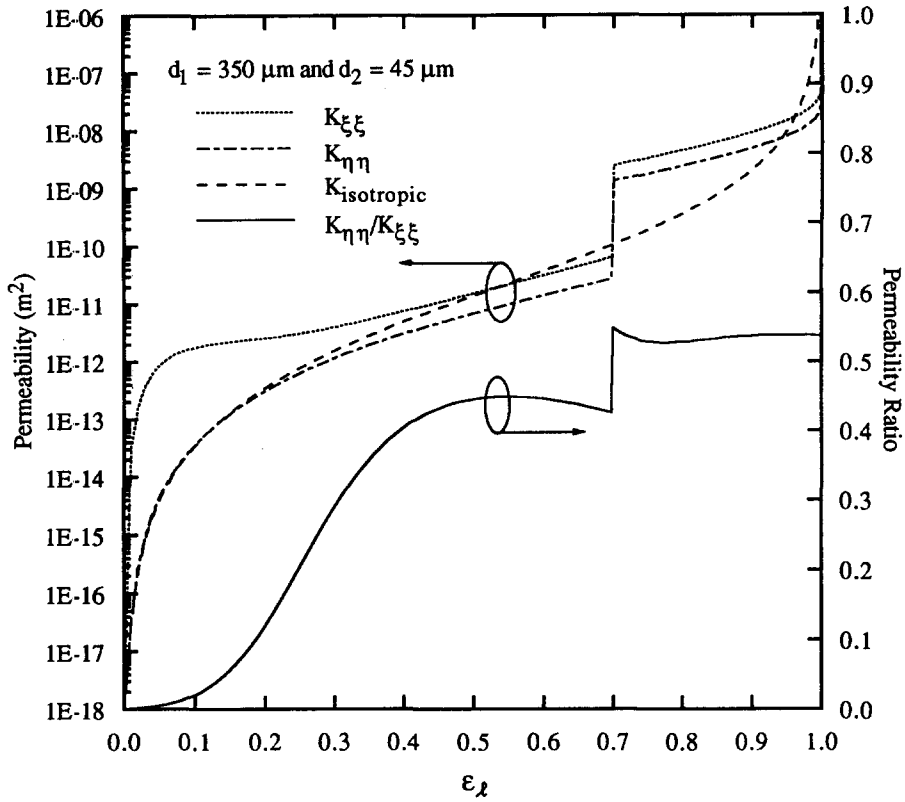

Fig. 2. Variation with liquid fraction of the permeabilities perpendicular, $K_{\eta\eta}$, and parallel, $K_{\xi\xi}$, to the primary dendrite arms, and of the approximate isotropic permeability. Also shown is the variation of the ratio of the perpendicular and parallel permeabilities.

Although this jump is obviously physically unrealistic, the development of a procedure for obtaining a smoother, physically realistic transition is beyond the scope of this study. Rather, the effects of this jump on the prediction of flow in the mushy zone will be illustrated in Section 4. Figure 2 also indicates that the permeability parallel to the primary arms is always larger than that perpendicular to the arms, although the two permeabilities only differ by a factor of around 2 over a large range of liquid fractions. However, Yoo and Viskanta [17] have shown that even such small differences in the permeabilities can have a significant effect on the prediction of flow structures and macrosegregation. Finally, Fig. 2 shows that the isotropic permeability is bracketed fairly well by the anisotropic permeabilities. The largest difference between the isotropic and anisotropic permeabilities is at high liquid fractions, where the analytical anisotropic permeabilities are used. Since the initiation of the formation of channels in the mushy zone occurs in regions where the liquid fraction is high, these differences can be significant.

3. NUMERICAL IMPLEMENTATION

The conservation equations presented in the previous section are equally valid in the fully solid, mushy and bulk liquid regions and can be solved using a fixed-grid, single-domain numerical solution procedure. Therefore, it is not necessary to track the liquid/mush or solid/mush interfaces, or to specify boundary conditions at these interfaces [1–3]. For the results in the following section, an implicit, control-volume-based finite-difference scheme has been used to discretize the conservation equations, and a power-law scheme used to evaluate the finite-difference coefficients. The velocity–pressure coupling in the momentum equations was handled using the SIMPLER algorithm [34].

The coupling of the energy and species conservation equations in the mushy zone through the phase diagram provides a method for calculating the solid volume fractions [35]. Briefly, the procedure to calculate ε_α or ε_γ before the eutectic point is reached is (with a detailed description found in Schneider and Beckermann [28]): (i) the temperatures and concentrations are assumed known, and the discretized form of the energy equation is solved for ε_α or ε_γ; (ii) the species conservation equations are solved for the average concentrations; (iii) the temperature for each location in the mushy zone is updated based on the liquidus temperature calculated using the average liquid concentration at that node. This procedure is repeated within each time step until convergence of the temperature, concentration and volume fraction fields is achieved. Once the eutectic point is reached, both the

α- and γ-solids form simultaneously while the temperature and concentrations remain fixed at the values given by the phase diagram. Then, the total $(\varepsilon_\alpha+\varepsilon_\gamma)$ solid fraction is calculated from the energy equation, and the α- and γ-solid fractions calculated from the liquid species conservation equation.

To account for the movement of the free surface in the riser, the height of the upper-most control volumes in the domain, i.e. those at the top of the riser in Fig. 1, was changed at each time step to assure global mass conservation. One can imagine this process as approximating the regression of the liquid surface down the riser. To be completely rigorous, the movement of the control volume faces should be accounted for in the discretization of the conservation equations. For simplicity that has not been done, but in the simulations presented here the volume change during any one time step was less than 0.005% so that this procedure is not expected to have a significant effect on the model predictions. In addition, to satisfy the assumption of no solid movement the solid densities were not allowed to vary in those control volumes that were completely solid.

Effort has been made to assure that the model and solution procedure are sound. Comparison of predictions of the model for diffusion-dominated (i.e. no fluid flow) solidification with the Neumann solution for isothermal phase change and with a semi-analytic solution for alloy solidification [36] showed good agreement. In addition, agreement was obtained between predictions of inverse segregation using the present model and results presented by Diao and Tsai [20]. Global conservation of mass and species was checked after each time step to assure there was no net loss or gain of these quantities in the domain. Finally, the computations were performed on a 50 by 65 grid that was biased near the walls, using a time step of 0.1 s. Based on previous experience with similar simulations, this grid and time step are fine enough to capture all of the fundamental transport phenomena while allowing for reasonable computational costs. Calculations have been successfully performed separately on Apollo DN10000, HP 715/50 and IBM 3090 computers. When using constant properties and a linear phase diagram, 1 s of simulation time required approximately 220 s of CPU time on an HP 715/50 workstation. For the variable properties and nonlinear phase diagram used here, computational times were considerably longer.

4. RESULTS AND DISCUSSION

The results of four different simulations are described:

- Case S1 (Scheil 1) assumes that there is no microscopic solid solute diffusion, i.e. equation (2) holds, and includes both buoyancy and contraction-driven flow.
- Case S2 (Scheil 2) is the same as Case S1, but the isotropic permeability function in Table 1 is used rather than the anisotropic permeabilities.
- Case S3 (Scheil 3) is the same as Case S1, but includes only contraction-driven flow.
- Case L1 (lever-rule 1) assumes complete microscopic solid solute diffusion, i.e. equation (1) holds, and includes both buoyancy and contraction-driven flow.

Detailed results from Case S1 will be presented, with results from Cases S2, S3 and L1 presented in parallel with those from Case S1 at appropriate points to facilitate comparison between the predictions. In the vector plots used to illustrate the simulation results, the velocity vectors represent $\langle \mathbf{v}_l \rangle^l$, the actual liquid velocity. Total solid volume fraction isopleths $(\varepsilon_s = \varepsilon_\alpha+\varepsilon_\gamma)$ are superimposed on the vector plots in 10% increments, with the location of the liquidus and solidus/eutectic fronts shown in bold. The shaded macrosegregation plots are of the mixture concentration, i.e. $C_{mix} = (\varepsilon_l\rho_l\langle C_l\rangle^l+\varepsilon_\alpha\rho_\alpha\langle C_\alpha\rangle^\alpha+\varepsilon_\gamma\rho_\gamma\langle C_\gamma\rangle^\gamma)/(\varepsilon_l\rho_l+\varepsilon_\alpha\rho_\alpha+\varepsilon_\gamma\rho_\gamma)$. Finally, the shaded eutectic fraction plots are of the sum of the α- and γ-solid fractions formed during the eutectic reaction (ε_e).

4.1. *Early stages of solidification*

Cooling at the left wall induces thermal buoyancy forces that establish a counter-clockwise natural convection cell in the melt for Cases S1, S2 and L1. In these cases, the first solid forms at the bottom of the cooled wall after about 80 s while in Case S3 the first solid forms after about 35 s. As time progresses, the mushy zone grows upward along the cooled wall and into the melt. After 150 s of cooling the mushy zone occupies approximately one-third of the cavity, and there are no completely solid regions. Figure 3 shows isotherms and liquid concentration isopleths for Case S1 after 150, 250 and 400 s of cooling. The formation of solid is accompanied by the enrichment of the interdendritic liquid with Sn, and since the density of Sn is smaller than that of Pb, this enrichment induces solutal buoyancy forces that oppose the thermal buoyancy forces driven by the temperature gradients shown in Fig. 3(a). The density of the solute enriched liquid is significantly less than the density of the liquid of initial composition, and, therefore, solutal buoyancy forces dominate in the mushy zone. The flow driven by these buoyancy forces carries the enriched liquid to the top of the cavity and into the bottom of the riser, as shown in Fig. 3(d). The enriched liquid is prevented from moving farther up the riser by convective flow in the riser which is due to both thermal buoyancy and feeding of the volume contraction.

Velocity and macrosegregation plots for Cases S1, S2 and L1 after 250 s of cooling are shown in Fig. 4. Figure 4(a) indicates that for Case S1 the mushy zone occupies approximately one-half of the cavity. By this time the flow is dominated by solutal buoyancy forces, the exceptions being a very small thermally driven cell in the lower right corner of the cavity and the com-

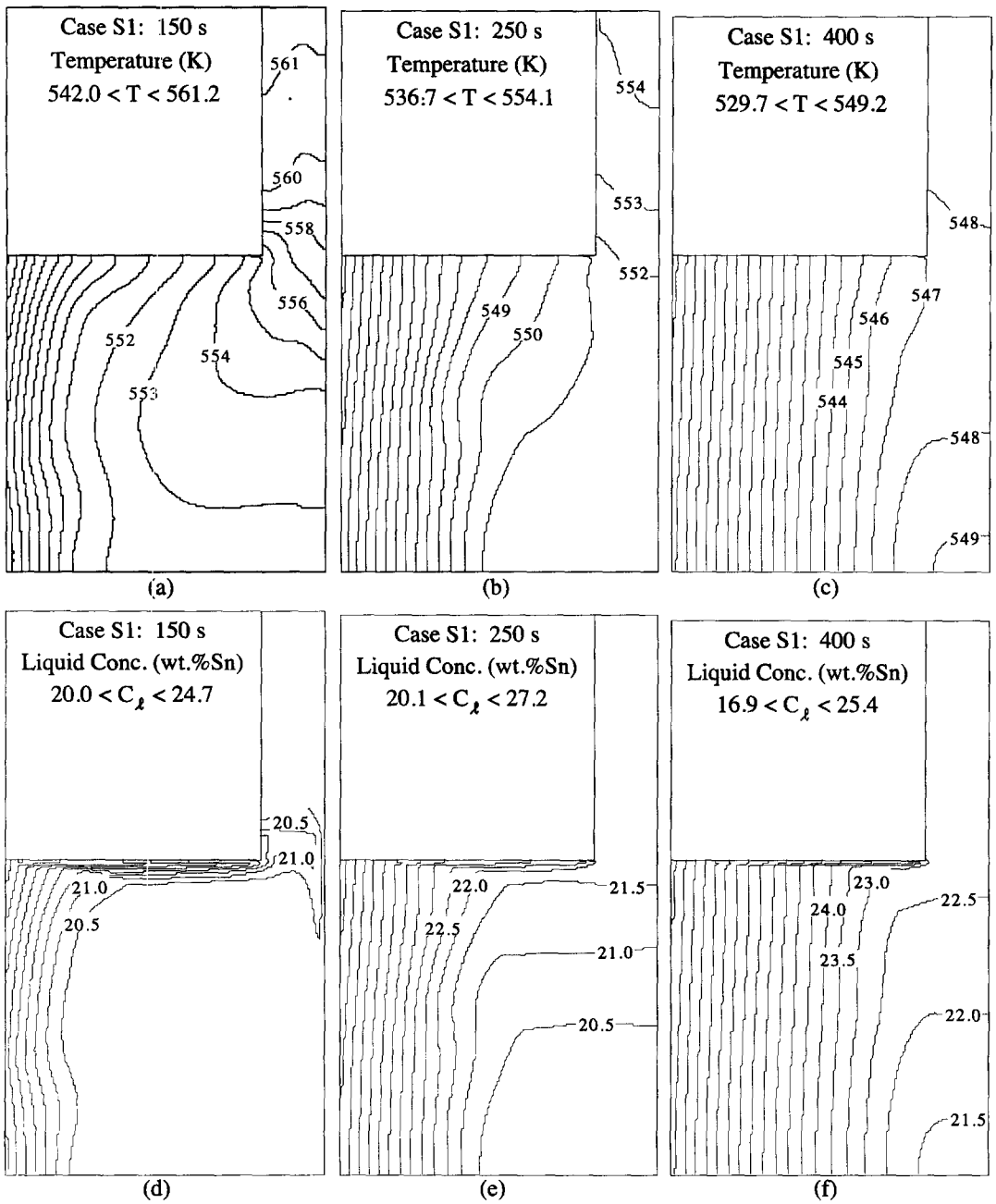

Fig. 3. Isotherms and liquid concentration isopleths for Case S1 at 150 s, 250 s and 400 s.

bined effects of buoyancy and contraction flow in the riser. Again, the upward flow in the mushy zone lifts the Sn-rich interdendritic liquid to the top of the cavity where, as shown in Figs. 3(e) and 4(d), it collects to form a thin layer. The liquidus temperature in this layer is depressed significantly by the high Sn concentration so that the mushy zone is confined to a small region near the cooled wall.

The velocity vectors and solid fraction isopleths for Case S1 (Fig. 4(a)) indicate the formation of channels in the upper portion of the mushy zone that are preferred paths for the upward flow of the Sn-rich interdendritic liquid. The presence of Sn-rich liquid in a channel (as indicated by Fig. 4(d)) lowers the liquidus temperature, and the advection of warm fluid into the region causes both remelting and the delayed formation of solid. In Fig. 4(a), it is also apparent that the flow in regions characterized by $\varepsilon_s < 30\%$ (approximately the right one-half of the mushy zone) is much stronger than in regions where the solid fraction is larger. The explanation for this behavior is the jump between the analytical and experimental permeability relations at $\varepsilon_l = 0.7$ discussed in Section 2.2. Obviously, such a jump is not physically realistic (in

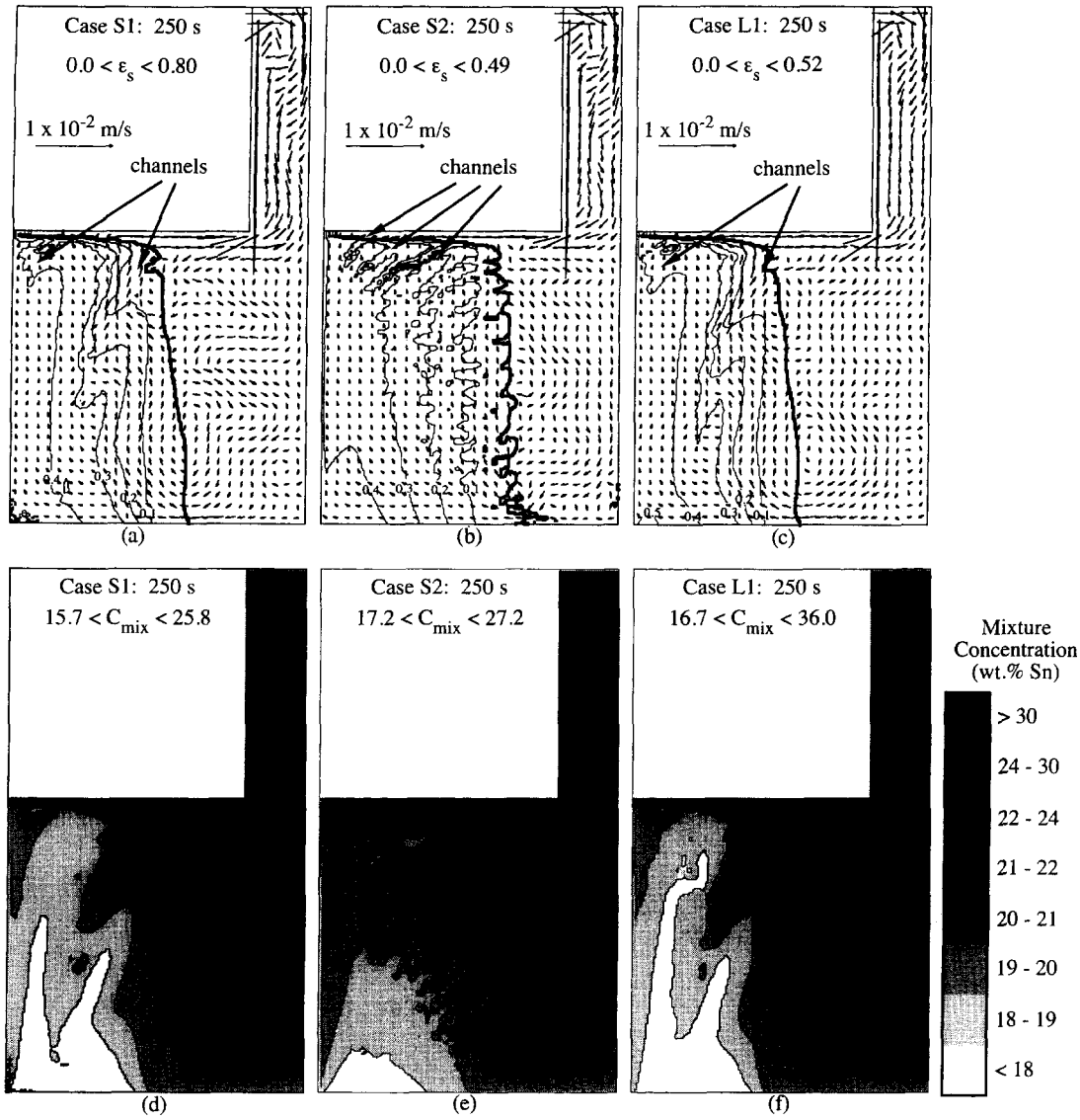

Fig. 4. Velocity field, solid fraction isopleths and macrosegregation for Cases S1, S2 and L1 at 250 s.

comparison with a smooth transition) and illustrates the need for continued work to develop permeability relations valid for all values of the liquid fraction.

Figures 4(b) and (e) show that, in comparison with Case S1, Case S2 predicts the formation of many short and more horizontally aligned channels. The isotropic permeability is much larger than the anisotropic permeabilities at high liquid fractions ($\varepsilon_l > 0.95$ in Fig. 2), so the resistance to flow is smaller near the edge of the mushy zone in Case S2, and many channels begin to form. Because the isotropic permeability decreases more rapidly than the anisotropic permeabilities ($0.7 < \varepsilon_l < 0.95$ in Fig. 2), the resistance to flow in Case S2 increases more rapidly leading to channels that are shorter. The relatively high permeabilities in Case S1 over a wide range of liquid fractions provide less resistance to upward, solutally driven flow, resulting in longer, vertically oriented channels. Figure 4(b) also shows that, because there is not a jump in the permeability in Case S2, there is a uniform variation in the velocities across the mushy zone. Finally, Fig. 4(e) indicates that macrosegregation in Case S2 is slightly less severe than in Case S1.

The predictions for Case S1 (Figs. 4(a) and (d)) and Case L1 (Figs. 4(c) and (f)) after 250 s of cooling are remarkably similar. This is somewhat surprising since Case S1 assumes that there is no solid solute diffusion microscopically in the solid while Case S2 assumes that the solid is microscopically well mixed. The discussion in Section 4.5 will show that the primary difference between the predictions of the two cases is in the amount of eutectic formed.

4.2. *Intermediate stages of solidification*

After 400 s of cooling in Case S1, Fig. 5(a) shows that the mushy zone occupies about three-quarters of

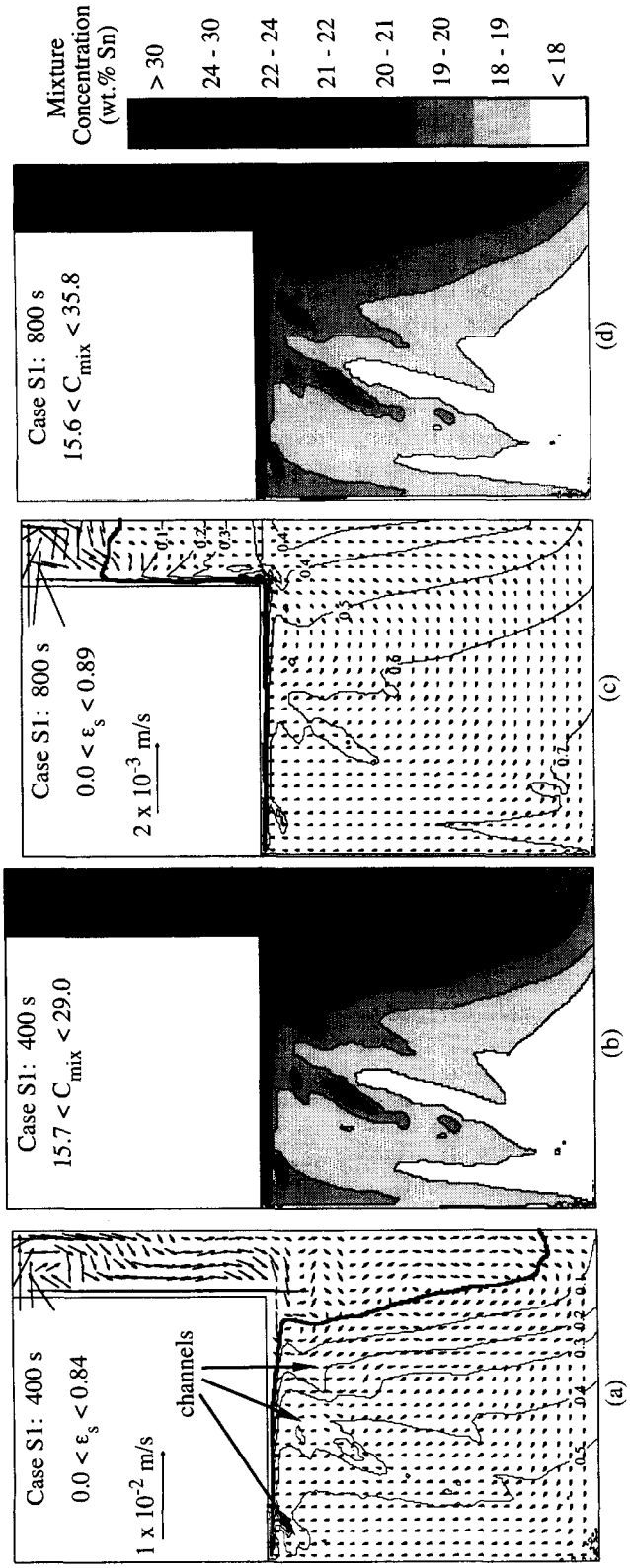

Fig. 5. Velocity field, solid fraction isopleths and macrosegregation for Case S1 at 400 s and 800 s.

the cavity. By this time the flow is slow enough that, as seen in Fig. 3(c), energy transport through much of the mushy zone is nearly conduction dominated. Figure 5(b) indicates that a third segregated channel has begun to form in the upper right portion of the mushy zone. The Sn-rich liquid at the top of the cavity, shown in Figs. 3(f) and 5(b), has kept the liquidus temperature low enough that the mushy zone is still confined to a small region near the cooled wall. Were it not for the fact that much of the Sn-rich liquid has been transported to the riser (as shown in Fig. 5(b)), it is expected that the Sn-rich layer at the top of the cavity would be much thicker and more severely segregated.

Figure 5(c) shows that after 800 s of cooling in Case S1 the mushy zone occupies nearly all of the cavity (except for part of the thin Sn-rich layer at the top) and two-thirds of the riser. A small solutally driven convection cell is contained in the top one-third of the riser, while the flow through the cavity is of a much smaller magnitude and is towards the cooled wall and the top of the cavity. The macrosegregation plot in Fig. 5(d) clearly shows the segregation in the channels that have formed in the mushy zone, as well as the small Sn-rich layer that extends from the top of the cavity along the left and into the top of the riser and the large Sn-deficient region at the bottom of the cavity.

4.3. *Final stages of solidification*

After about 1700 s of cooling for Case S1, eutectic (both α- and γ-) solid begins to form along the cooled wall. Since by this time energy transport across the cavity is conduction dominated, the eutectic front (i.e. the eutectic isotherm) remains nearly straight and vertical as it moves across the cavity. Figure 6(a) shows that after 1800 s the eutectic front has progressed to approximately the midpoint of the cavity, and the rest of the domain is occupied by mush. This figure also shows that the flow is dominated by the solid/liquid density change on solidification. Figure 6(b) shows the flow field and eutectic front for Case S2 after 1800 s of cooling, and comparing with Fig. 6(a) it is obvious that the behavior during the final stages of solidification is similar for Cases S1 and S2. For both cases solidification of the cavity was complete after 2050 s.

The velocity field and the position of the solidus/eutectic front for Case L1 after 2050 s of cooling in Fig. 6(c) indicates that the final stages of solidification for this case are quite different. Similar to Cases S1 and S2, the first completely solid regions began to form after about 1700 s, but in Case L1 the solid was in the Sn-poor area at the bottom of the cavity (not at the cooled wall) and contained only α-phase (no eutectic) solid. In fact, no eutectic solid was formed until after 2000 s. Since much of the fully solid region in Fig. 6(c) contains no eutectic, at this time the boundary between the mushy and solid regions is not the eutectic isotherm. Note that the liquid level in the riser is higher in Fig. 6(c) than in Fig. 6(a) due to the use of different microsegregation models for Cases L1 and S1. The different average solid concentrations and eutectic solid fractions predicted when using the different microsegregation models affect the predicted solid densities which, in turn, lead to differences in the amount of liquid needed to feed the solidification shrinkage [14]. In Case L1, after about 2100 s the remaining liquid has a high enough concentration that eutectic solid forms from it, and the cavity completely solidifies after 2190 s.

4.4. *Final macrosegregation distributions*

Figure 7 shows the final macrosegregation patterns for all of the cases. It is interesting to first compare the macrosegregation plots for Case S1 after 800 s (Fig. 5(d)) and 2050 s (Fig. 7(a)). Close examination reveals that the size of all the Sn-deficient regions has decreased. The reason for these changes is the continuous drawing of Sn-rich liquid from the top of the cavity and the riser into the rest of the cavity by contraction-driven flow.

Comparing the final macrosegregation plot for Case S2 (Fig. 7(b)) with that for Case S1 shows that, as before, the most obvious difference between the predictions for these cases is in the number, length and orientation of the channels. Figure 7(c) shows that in Case S3 shrinkage-driven flow has transported solute from the Sn-deficient region in the riser and redistributed it throughout the cavity, where the composition is slightly higher than the original. In comparison with the cases that include buoyancy-driven flow, the magnitude of segregation for Case S3 is very small. A comparison of the plots in Figs. 7(a) and (d) shows that the final macrosegregation patterns for Cases S1 and L1 are again very similar. Closer examination reveals that the extent of macrosegregation is slightly worse for Case L1. This is seen, for instance, in the size of the Sn-poor region at the bottom of the cavity and in the presence of a small Sn-rich region at the lower right wall. By comparison, Voller *et al.* [3] observed that segregation was more severe when there was assumed to be no microscopic solid solute diffusion (S1) rather than complete microscopic solute diffusion (L1) when simulating the solidification of an NH_4Cl–H_2O solution.

To further illustrate the differences in macrosegregation predicted by the different cases, Fig. 8 shows the final macrosegregation profiles along the horizontal and vertical midsections of the cavity, with the behavior at the left wall and top of the cavity shown in more detail in Figs. 8(a) and (d) respectively. Figure 8(b) shows that, in general, the three cases that involve buoyancy flow predict similar macrosegregation distributions, and the variations in macrosegregation for these cases are much larger than those predicted for contraction-driven flow only (S3). Because of the small overall heat transfer coefficient used to cool the left wall [24], the inverse segregation predicted by Case S3 is barely visible. Case S1 shows the largest jump in the mixture concentration across

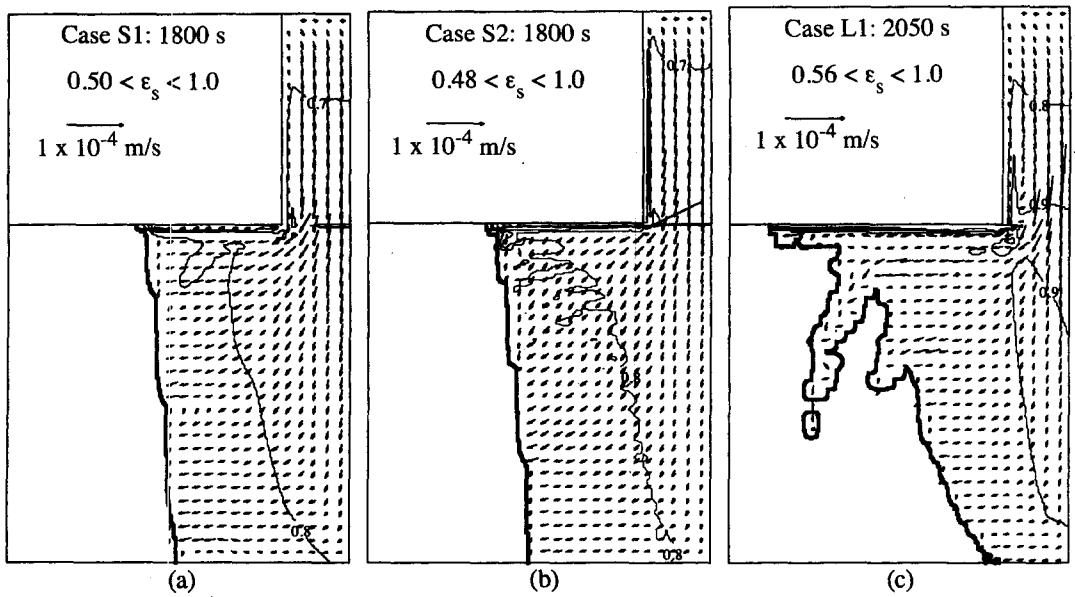

Fig. 6. Velocity field, solid fraction isopleths and eutectic/solidus front for Cases S1, S2 and L1 near the end of solidification.

the cavity, while Case S2 shows many smaller variations in the mixture concentration, all of which correspond to one of the channels seen in the macrosegregation plots. Case S2 also shows a much narrower band of positive segregation near the right wall and overall shows the least severe segregation. Finally, Fig. 8(b) indicates that Case L1 predicts slightly more severe segregation (both positive and negative) than Case S1, indicating that the extent of macrosegregation predicted by the limiting microsegregation cases is slightly different.

Examining Figs. 8(c) and (d) shows that the extent of macrosegregation along the vertical centerline of the cavity is nearly the same for the three cases with buoyancy flow, and as expected, there is little variation in the profile for the contraction flow case. As in Fig. 8(b), Case S2 shows many small variations in the mixture concentration corresponding to the many small channels predicted by this case, and Case L1 shows the most severe negative segregation. Figure 8(d) shows the extremely high positive segregation found at the top of the cavity for the cases with buoyancy driven flow. If some of the Sn-rich fluid had not been allowed to escape into the riser, one would expect that this layer would be much thicker and more severely segregated.

A final examination of Fig. 8(a) shows that all of the cases predict a narrow band of negative segregation very near the cooled wall. Because this segregation is apparent for Case S3, the cause cannot be buoyancy driven flow. To further investigate the reason for this negative segregation, Fig. 9 shows macrosegregation profiles predicted by the present model when the same alloy is solidified unidirectionally, using the same initial and boundary conditions, and assuming that equation (2) holds. The curves in Fig. 9 correspond to three different cases: the full model with no buoyancy-driven flow; the full model with no buoyancy-driven flow and no macroscopic species diffusion in the liquid; and the full model with the solid and liquid densities equal, i.e. no buoyancy or contraction driven flow. Figure 9(b) shows that, as expected, the two cases that include contraction-driven flow predict the formation of a typical *positive* inverse segregation pattern [14, 19–21, 24] (due to the continual influx of higher concentration liquid to compensate for solidification shrinkage), while the case with no flow shows a nearly uniform mixture concentration across most of the casting. Figure 9(a) indicates that, although there is no mixture concentration gradient at the impermeable wall, an extremely narrow *negatively* segregated band very near the chill is present when species diffusion in the liquid is included. Because of cooling at the chill, there is a positive temperature gradient in the melt, and because the temperature and liquid concentration are coupled through the liquidus line of the phase diagram, there is a corresponding negative concentration gradient in the liquid, with the concentration decreasing from a maximum at the wall (although there is no gradient at the impermeable wall) to the initial concentration far from the chill. (Note that Fig. 9 shows the mixture, not the liquid, concentration.) As the wall is impermeable, macroscopic (but short range) solute diffusion due to this liquid concentration gradient causes the liquid near the chill to become depleted of solute (in comparison to a case with no macroscopic solute diffusion). Solid

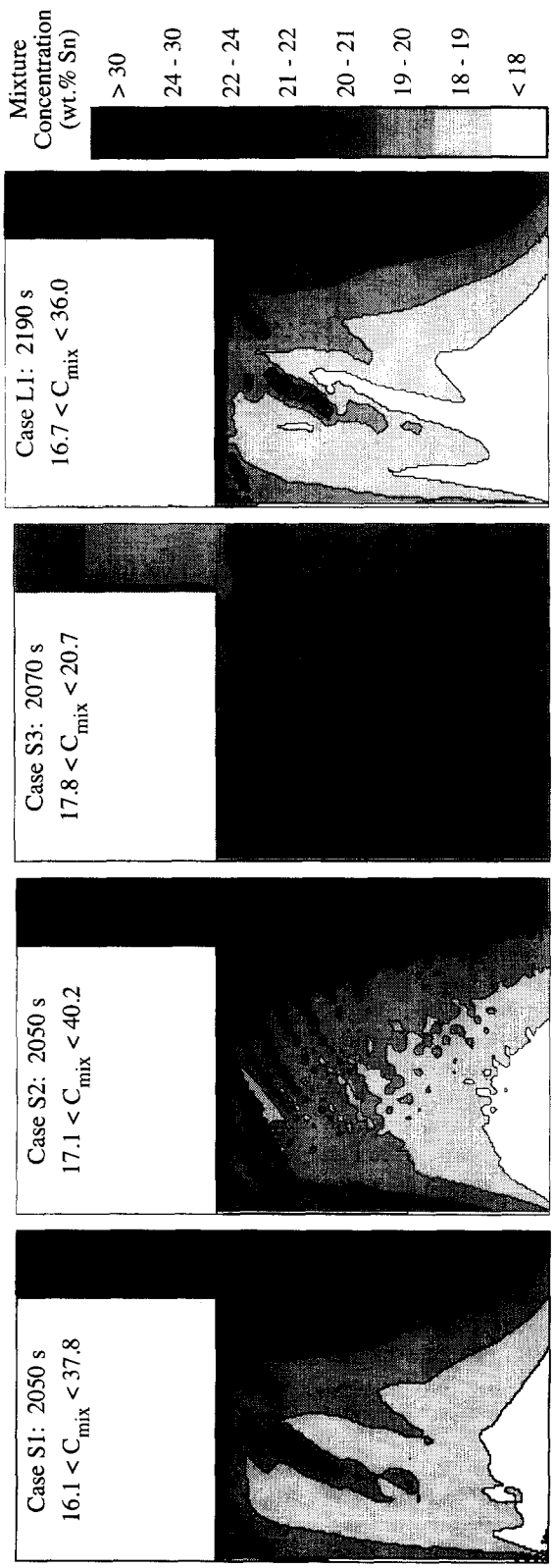

Fig. 7. Final macrosegregation patterns for Cases S1, S2, S3 and L1.

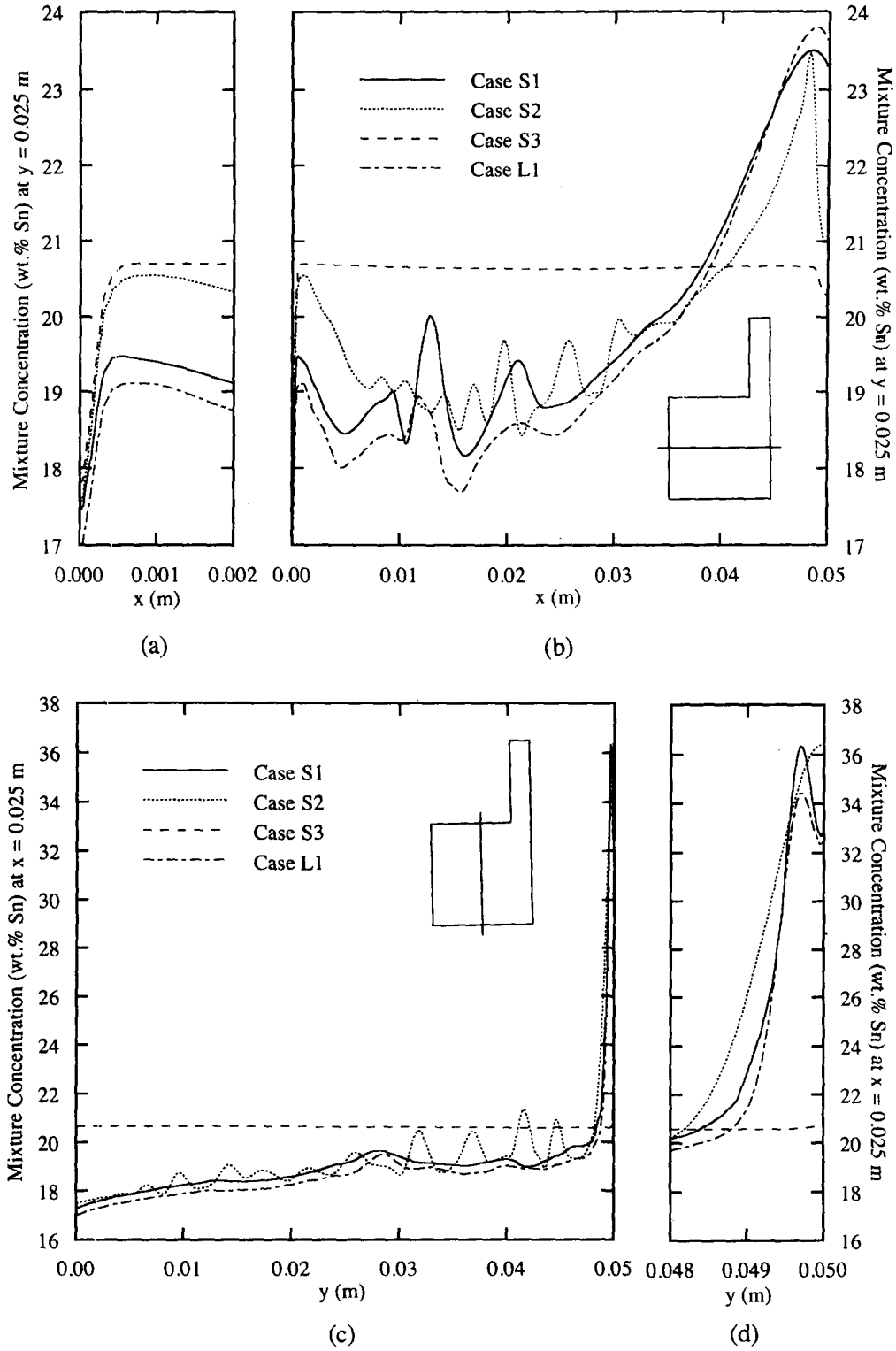

Fig. 8. Final macrosegregation profiles: (a) and (b) along $y = 0.025$ m, and (c) and (d) along $x = 0.025$ m.

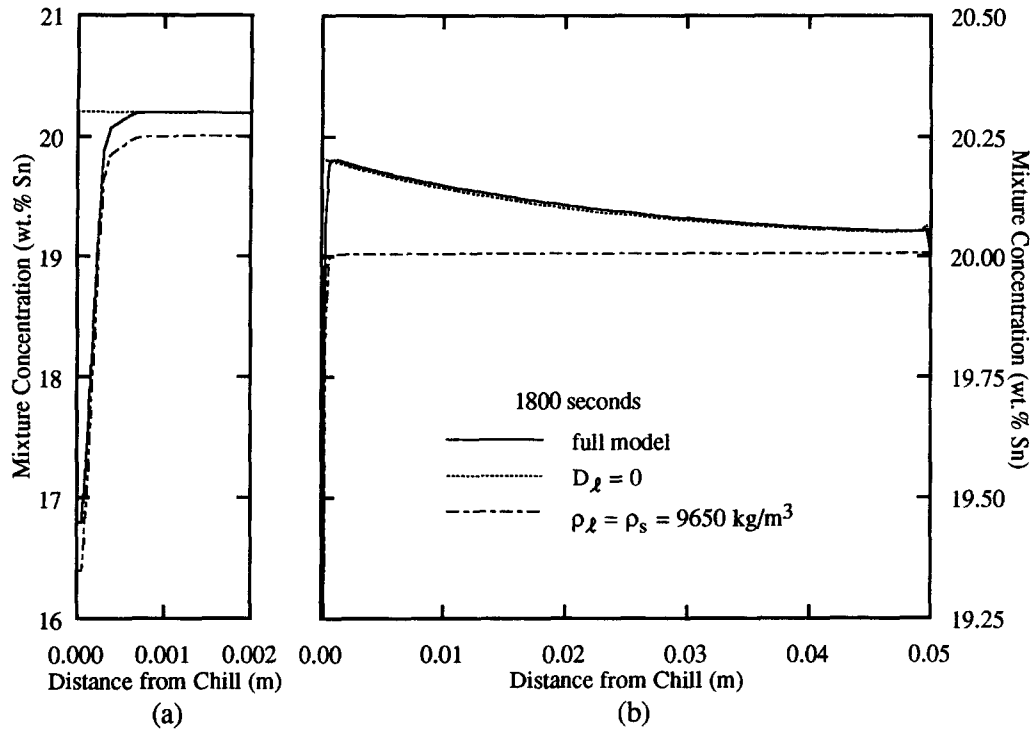

Fig. 9. Macrosegregation profiles for unidirectional solidification with no buoyancy-driven flow: (a) near the chill and (b) throughout the casting.

that forms from this liquid consequently has a lower composition, which leads to a lower mixture concentration in a small band near the chill, as seen in Figs. 8(a) and 9(a). The width of the band is small due to the small macroscopic mass diffusivity in the liquid, i.e. the band would be wider and more severely segregated if the mass diffusivity were higher.

4.5. *Final eutectic fraction distributions*

Figure 10 contains shade plots that show the final eutectic volume fractions predicted for all of the cases. Comparing Figs. 10(a) through (c) with Figs. 7(a) through (c) shows that for Cases S1, S2 and S3 the final macrosegregation and eutectic fraction patterns are very similar, with more eutectic formed where positive segregation is largest, e.g. in the channels and at the top of the cavity in Case S1. It is important to note that for Cases S1 and S2 there is no fully solid region that contains less than 5% eutectic by volume. Figure 10(d), however, shows that for Case L1 a large portion of the solid in the cavity contains little or no eutectic, with eutectic found only in regions that are severely segregated. The Scheil and lever-rule models (along with properties for the Pb–Sn system) would predict eutectic volume fractions of about 25% and 5% respectively. Since Cases S1 and L1 would reduce to those two models if macroscopic species transport was neglected, the differences between Figs. 10(a) and (d) are not surprising. These results are also consistent with the observations of Felicelli *et al.* [5] for diffusion-dominated solidification.

5. CONCLUSIONS

The combined effects of microsegregation, mushy zone permeability and flow, caused by contraction and thermosolutal convection, on the prediction of macrosegregation and eutectic fraction during the solidification of a Pb-20 wt% Sn alloy have been evaluated. The results illustrate the coupled nature of these phenomena and indicate the sensitivity of model predictions to some assumptions often used in deriving macroscopic solidification models.

For the situation considered here, predicted macrosegregation patterns for two limiting cases of microsegregation (either complete or no microscopic solid solute diffusion) were similar, with only slightly more severe segregation predicted with complete solute diffusion (lever-rule type model). However, the Scheil type microsegregation model (no microscopic solid solute diffusion) predicted the formation of a significant eutectic fraction throughout the casting, while the lever-rule type model predicted the formation of a small amount of eutectic only in regions of severe positive segregation. Macrosegregation resulting from contraction-driven flow (caused by solid/liquid density differences as well as density variations with both temperature and concentration) was overwhelmed by that caused by thermosolutal convection (because of the low cooling rate used here [24]). However, differences in the predicted average solid concentrations and eutectic fractions when using the two limiting cases of solid microsegregation led to differences in

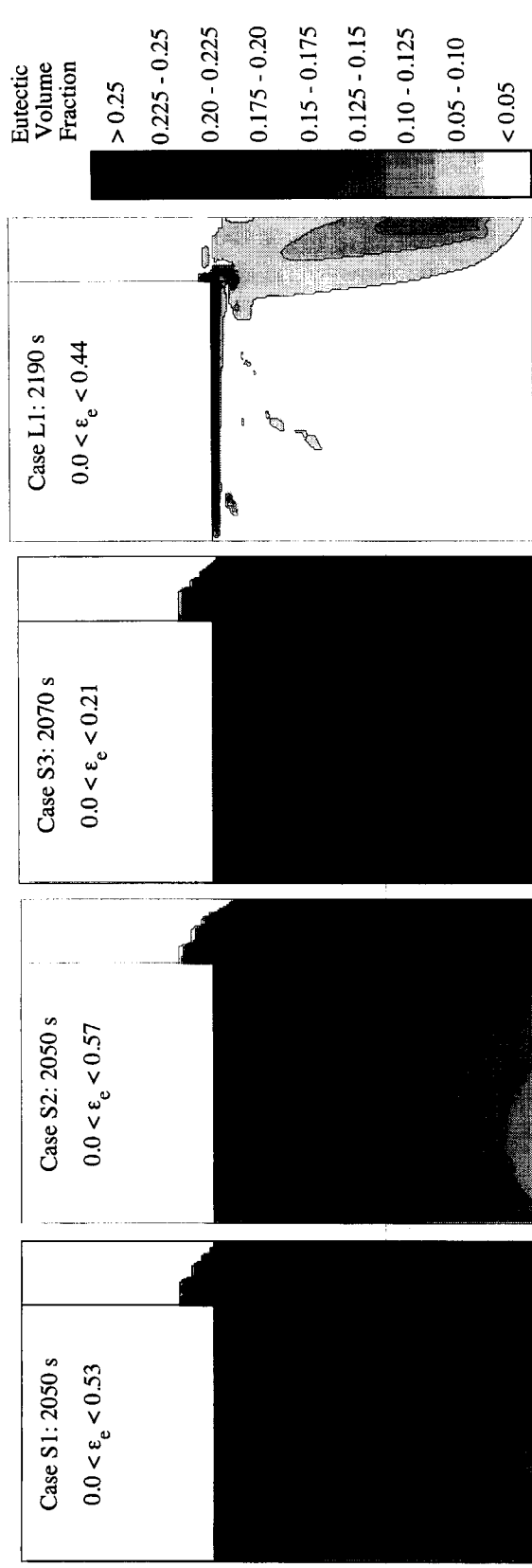

Fig. 10. Final eutectic fraction distributions for Cases S1, S2, S3 and L1.

the predicted solid density distributions. This, in turn, affected the prediction of contraction-driven flow. These results indicate that if one is solely interested in macrosegregation due to buoyancy driven flow, it may not be necessary to use more complicated microsegregation models (e.g. including finite rate solute diffusion in the solid microscopically or more carefully incorporating coarsening effects). However, if one is interested in predicting eutectic distributions and/or if contraction-driven flow is significant, a more accurate microsegregation model is probably necessary. Careful comparison of predicted and measured macrosegregation and eutectic fraction distributions for a wide range of cooling rates is clearly necessary to both validate the model predictions and to determine whether using limiting cases of microsegregation is sufficient.

Using two different permeability functions available in the literature, it was determined that when the mushy zone permeability is relatively high for large liquid fractions, the resulting predictions show long, more vertically oriented channels. For lower permeabilities, shorter and more horizontally oriented channels were predicted. Since the uncertainty in experimentally measured permeabilities is large, and especially since no experimental measurements have been made for high liquid fractions, these results show a definite need for further investigation into the permeability of mushy zones. The present results suggest that information on the mushy zone permeability could be worked out from solidification experiments by measuring the length and orientation of the channels in a solidified sample, and using model predictions to determine what type of permeability (e.g. degree of anisotropy, relative magnitude, etc.) is necessary to predict similar channels. It should also be noted that the present results are limited to two dimensions, while the formation of channels is inherently a three-dimensional phenomena [37]. That is, three-dimensional simulations may be necessary to predict accurately the formation of what are, in reality, rod-like channels in the mushy zone.

Acknowledgments—This work was supported by the National Science Foundation under grant no. CTS-8957149.

REFERENCES

1. W. D. Bennon and F. P. Incropera, The evolution of macrosegregation in statically cast binary ingots, *Met. Trans. B.* **18B,** 611–616 (1987).
2. C. Beckermann and R. Viskanta, Double-diffusive convection during dendritic solidification of a binary mixture, *PhysicoChem. Hydrodyn.* **10,** 195–213 (1988).
3. V. R. Voller, A. D. Brent and C. Prakash, The modelling of heat, mass and solute transport in solidification systems, *Int. J. Heat Mass Transfer* **32,** 1719–1731 (1989).
4. G. Amberg, Computation of macrosegregation in an iron–carbon cast, *Int. J. Heat Mass Transfer* **34,** 217–227 (1991).
5. S. D. Felicelli, F. C. Heinrich and D. R. Poirier, Simulation of freckles during vertical solidification of binary alloys, *Met. Trans. B* **22B,** 847–859 (1991).
6. P. J. Prescott and F. P. Incropera, Numerical simulation of a solidifying Pb–Sn alloy : the effects of cooling rate on thermosolutal convection and macrosegregation, *Met. Trans. B* **22B,** 529–540 (1991).
7. D. G. Nielson and F. P. Incropera, Effect of rotation on fluid motion and channel formation during unidirectional solidification of a binary alloy, *Int. J. Heat Mass Transfer* **36,** 489–503 (1993).
8. D. Xu and Q. Li, Numerical method for solution of strongly coupled binary alloy solidification problems, *Numer. Heat Transfer* **20A,** 181–201 (1991).
9. H. Shahani, G. Amberg and H. Fredriksson, On the formation of macrosegregations in unidirectionally solidified Sn–Pb and Pb–Sn alloys, *Met. Trans. A* **23A,** 2301–2311 (1992).
10. M. C. Schneider and C. Beckermann, Effects of simplified enthalpy relations on the prediction of heat transfer during solidification of a lead–tin alloy, *Appl. Math. Modelling* **15,** 596–605 (1991).
11. D. R. Poirier, P. J. Nandapurkar and S. Ganesan, The energy and solute conservation equations for dendritic solidification, *Met. Trans. B,* **22B,** 889–900 (1991).
12. D. R. Poirier, and P. J. Nandapurkar, Enthalpies of a binary alloy during solidification, *Met. Trans. A* **19A,** 3057–3061 (1988).
13. D. R. Poirier, Densities of Pb–Sn alloys during solidification, *Met. Trans. A* **19A,** 2349–2354 (1988).
14. S. Sundarraj and V. R. Voller, A dual scale model of segregation phenomena, *ASME Transport Phenomena in Solidification,* **HTD-284,** 29–42 (1994).
15. D. R. Poirier, Permeability for flow of interdendritic liquid in columnar-dendritic alloys, *Met. Trans. B* **18B,** 245–255 (1987).
16. S. K. Sinha, T. Sundarajan and V. K. Garg, A variable property analysis of alloy solidification using the anisotropic porous medium approach, *Int. J. Heat Mass Transfer* **35,** 2865–2877 (1992).
17. H. Yoo and R. Viskanta, Effect of anisotropic permeability on the transport process during solidification of a binary mixture, *Int. J. Heat Mass Transfer* **35,** 2335–2346 (1992).
18. K. C. Chiang and H. L. Tsai, Interaction between shrinkage-induced fluid flow and natural convection during alloy solidification, *Int. J. Heat Mass Transfer* **35,** 1771–1778 (1992).
19. J. H. Chen and H. L. Tsai, Inverse segregation for a unidirectional solidification of aluminum–copper alloys, *Int. J. Heat Mass Transfer* **36,** 3069–3075 (1993).
20. Q. Z. Diao and H. L. Tsai, Modeling of solute redistribution in the mushy zone during solidification of aluminum–copper alloys, *Met. Trans. A* **24A,** 963–973 (1993).
21. Q. Z. Diao and H. L. Tsai, The formation of negative and positive segregated bands during solidification of aluminum–copper alloys, *Int. J. Heat Mass Transfer* **36,** 4299–4305 (1993).
22. D. Xu and Q. Li, Gravity- and solidification-shrinkage-induced liquid flow in a horizontally solidified alloy ingot, *Numer. Heat Transfer A* **20A,** 203–221 (1991).
23. D. Xu, Q. Li and R. D. Pehlke, Computer simulation of Al–Cu alloy solidification using a continuum model, *AFS Trans.* **91,** 737–745 (1991).
24. M. J. M. Krane and F. P. Incropera, Analysis of the effect of shrinkage on macrosegregation in alloy solidification, *ASME Transport Phenomena in Solidification,* **HTD-284,** 13–27 (1994).
25. J. Ni and C. Beckermann, a two-phase model for mass, momentum, heat and species transport during solidification, *Met. Trans. B* **22B,** 349–361 (1990).
26. M. C. Schneider, Modeling the columnar dendritic solidification of lead–tin alloys, M. S. Thesis, The University of Iowa, Iowa City (1991).

27. C. Beckermann and R. Viskanta, Mathematical modeling of transport phenomena during alloy solidification, *Appl. Mech. Rev.* **46,** 1–27 (1993).
28. M. C. Schneider and C. Beckermann, Summary of a method for numerically simulating the columnar dendritic solidification of binary alloys, Technical Report UIME-CB01-1993, Dept. of Mechanical Engineering, The University of Iowa, Iowa City (1993).
29. C. Y. Wang and C. Beckermann, A multiphase solute diffusion model for dendritic alloy solidification, *Met. Trans. A* **24A,** 2787–2802 (1993).
30. W. Kurz and D. J. Fisher, *Fundamentals of Solidification* (3rd Edn). Trans Tech, Aedermannsdorf, Switzerland (1989).
31. M. Rappaz and V. R. Voller, Modeling of micro-macrosegregation in solidification processes, *Met. Trans. A* **21A,** 749–753 (1990).
32. J. E. Drummond and M. I. Tahir, Laminar viscous flow through regular arrays of parallel solid cylinders, *Int. J. Multiphase Flow* **10,** 515–540 (1984).
33. A. S. Sangani and A. Acrivos, Slow flow past periodic arrays of cylinders with application to heat transfer, *Int. J. Multiphase Flow* **8,** 193–206 (1982).
34. S. V. Patankar, *Numerical Heat Transfer and Fluid Flow*. McGraw-Hill, New York (1980).
35. C. Prakash and V. R. Voller, On the numerical solution of continuum mixture model equations describing binary solid liquid phase change, *Numer. Heat Transfer* **15,** 171–189 (1989).
36. V. R. Voller, Development and application of a heat balance integral method for analysis of metallurgical solidification, *Appl. Math. Modelling* **13,** 3–11 (1989).
37. D. G. Nielson and F. P. Incropera, Three-dimensional considerations of unidirectional solidification in a binary liquid, *Numer. Heat Transfer A* **23A,** 1–20 (1993).
38. Y. S. Touloukain, R. W. Powell, C. Y. Ho and P. G. Klemens, *Thermophysical Properties of Matter*, Vol. 1. IFI/Plenum, New York (1970).
39. H. R. Thresh and A. F. Crawley, The viscosities of lead, tin and Pb–Sn alloys, *Met. Trans.* **1,** 1531–1535 (1970).
40. N. Streat and F. Weinberg, Macrosegregation during solidification resulting from density differences in the liquid, *Met. Trans.* **5,** 2539–2548 (1974).
41. C. M. Klaren, J. D. Verhoeven and R. Trivedi, Primary dendrite spacing of lead dendrites in Pb–Sn and Pb–Au alloys, *Met. Trans. A* **11A,** 1853–1861 (1980).
42. S. N. Tewari and R. Shah, Thermosolutal convection during dendritic growth and its effect on macrosegregation, *Micro-Macro Scale Phenomena in Solidification*, **HTD-218,** 9–16 (1992).
43. A. Roosz, E. Halder and H. E. Exner, Numerical calculation of microsegregation in coarsened dendritic microstructures, *Mater. Sci. Technol.* **2,** 1149–1155 (1986).